Structural Transformation of Pt–Ni Nanowires as Oxygen Reduction Electrocatalysts to Branched Nanostructures during Potential Cycles

Masaru Kato,*[,1,2] Yoshimi Iguchi,[2] Tianchi Li,[2] Yuta Kato,[2] Yu Zhuang,[2] Kotaro Higashi,[3] Tomoya Uruga,[3,4] Takahiro Saida,[5] Keiko Miyabayashi,[6] Ichizo Yagi*[,1,2]

[1]Faculty of Environmental Earth Science, Hokkaido University, N10W5, Kita-ku, Sapporo 060-0810, Japan

[2]Graduate School of Environmental Science, Hokkaido University, N10W5, Kita-ku, Sapporo 060-0810, Japan

[3]Innovation Research Center for Fuel Cells, The University of Electro-Communications, Chofugaoka, Chofu, Tokyo 182-8585, Japan

[4]Japan Synchrotron Radiation Research Institute, SPring-8, Sayo, Hyogo 679-5198, Japan

[5]Department of Applied Chemistry, Meijo University, Nagoya 468-8502, Japan

[6]Graduate School of Integrated Science and Technology, Shizuoka University, 3-5-1, Naka-ku, Hamamatsu 432-8561, Japan

KEYWORDS. Nanowires, oxygen reduction reaction, in situ X-ray absorption spectroscopy, polymer electrolyte fuel cell, branched nanostructures, Ostwald ripening, phase engineering of nanomaterials.

ABSTRACT. We report the preparation, oxygen reduction reaction (ORR) electrocatalytic activity, and structural transformation of Pt–Ni nanowires (NWs) during potential cycles in the presence and absence of Pt–Ni nanoparticles (NPs). The ORR activity of NWs increases over the 25000 potential cycles in the presence of NPs involving the structural transformation of NWs to branched nanostructures assisted by Ostwald ripening of NPs. This structural transformation is coupled with the surface electronic structural change, confirmed by *in situ* X-ray absorption spectroscopy and carbon monoxide stripping voltammetry, leading to catalytic activity improvement and Pt dissolution suppression. Although a similar structural transformation was also observed even in the absence of NPs, more amounts of Pt were dissolved during potential cycles. These results indicate that the structural transformation is intrinsic to Pt-based NWs but the structural transformation of NWs assisted by Ostwald ripening of NPs is beneficial to suppress the Pt dissolution. The concept of the structural optimization of nanostructures catalysts assisted by Ostwald ripening of NPs under potential cycles will guide us to develop highly active and durable Pt-based electrocatalysts and phase-engineered nanomaterials.

Oxygen reduction reaction (ORR) is the key reaction in polymer electrolyte fuel cells (PEFCs) and metal–air batteries. The ORR requires electrocatalysts and limits the overall performance of these devices and batteries. Platinum-group metals (PGMs) are widely used as ORR electrocatalysts in PEFCs because platinum is the most active ORR catalyst in the metals. To improve the ORR electrocatalytic activity of PGM-based electrocatalysts, Pt–M alloy (M = Ni or Co) and nanostructured catalysts such as core–shell nanoparticles,[1] nanoframes[2-6] and nanowires (NWs)[7-13] have been studied. These nanostructured catalysts show high initial activity and some of them are already used in practical PEFC in fuel cell vehicles and electricity generators.

The challenge for developing next-generation PGM electrocatalysts is to develop highly durable ORR electrocatalysts under a harsh operation condition: potential changes in acidic environments, which can be provided from polymer electrolytes possessing sulfonic acid groups. In this condition, many electrochemical events occur at the catalyst/support interface: for example, platinum dissolution/redeposition, dealloying, Ostwald ripening, agglomeration, and electromigration.[14-15] These undesirable reactions are facilitated by heterointerfaces or grain boundaries of PGM electrocatalysts particularly for Pt nanoparticles (NPs) on carbon supports, leading to electrocatalyst degradation.[1,5,16] Thus, we need to design and develop next-generation PGM electrocatalysts considering minimizing or even utilizing these degradation processes to develop highly durable electrocatalysts.

Herein, we report the preparation, ORR electrocatalytic activity, and durability of Pt–Ni NWs in the presence and absence of NPs. Pt-based NWs have been intensively studied as ORR catalysts because of their high mass activity.[7,17] One-dimensional NWs with large contact areas with the support are known to suppress metal dissolution, agglomeration, and Ostwald ripening, compared with zero-dimensional NPs.[7,10-11,17] In this work, the structural transformation of Pt–Ni NWs to branched nanostructures have been observed in the presence and absence of NPs, involving the surface

and electronic structural changes, confirmed by scanning transmission electron microscopy (STEM) and physicochemical measurements including *in situ* X-ray absorption spectroscopy (XAS).

Pt–Ni NWs were prepared from the precursor mixture of [$Pt(acac)_2$] (acac = acetylacetonate), [$Ni(acac)_2$], glucose, [$Mo(CO)_6$], and cetyltrimethylammonium chloride (CTAC) in oleylamine at 433 K under Ar for 2 h (NW_{Ar}) and then immobilized on a carbon black of Vulcan XC-72 (NW_{Ar}/C, See the detail in the Supporting Information).[8-9] STEM and high-angle annular dark-field (HAADF)-STEM observation of the as-prepared product revealed the formation of nanowires with an average diameter of 1.92±0.04 nm and an average length of 46±3 nm (**Figures 1a, 1b**, **S1a** and **S1b**). An aspect ratio of NWs can be calculated to be ca. 24. Note that NPs with an average diameter of 6.7±0.3 nm (**Figure S1c**) were also co-present when NWs were prepared under Ar. Counting the number of NWs and NPs in HAADF-STEM images of the as-prepared NW_{Ar}/C allowed us to determine the ratio of the number of NWs to that of NPs to ca. 1:1 (**Figure S2**). Energy dispersive X-ray spectroscopy (EDS) analysis allowed us to confirm Pt–Ni@Ni core–shell NPs (**Figure S3**). Because NWs were grown by the oriented attachment mechanism and Ostwald ripening process of NPs,[9,13,18-20] it is most likely that NPs that were not used for the growth of NWs remained in an inert atmosphere. Inductively coupled plasma mass spectroscopy (ICP–MS) measurements of the product confirmed a Pt:Ni atomic ratio of 52:48 for the as-prepared product. Powder X-ray diffraction (PXRD) patterns of the as-prepared NWs indicate the representative face-centered cubic (fcc) structure and showed a characteristic 111 diffraction peak (**Figure S4**). Although the peak-top position of this peak was slightly shifted to higher angles than that of Pt/C, it was much lower than the position that can be predicted by the Vegard's law[21] for Pt–Ni random alloy NWs with the Pt:Ni atomic ratio of 52:48 ($2\theta \sim 42.02^{\circ}$). This result suggests that Pt–Ni NWs with low Ni-doping amounts and most of the Ni atoms are possibly placed on the surface of ultrathin Pt NWs, as previously reported.[7,10,13,20]

The surface deposition of Ni is also supported by the drastic change of Pt:Ni atomic ratios after an electrochemical cleaning process in a 0.1 M $HClO_4$ aqueous solution under Ar: ca. 96% of Ni in the initial NW_{Ar}/C was leached into the electrolyte solution after 100 potential cycles between +0.05 and +1.20 V vs. RHE under Ar, which is an electrochemical cleaning process and done for each electrochemical measurement in this work. This electrochemical cleaning process yielded the Pt:Ni atomic ratio of 94:6, which was confirmed by ICP-MS. Most of the Ni atoms are placed on Pt NWs and, therefore, susceptible to the electrochemical leaching process.

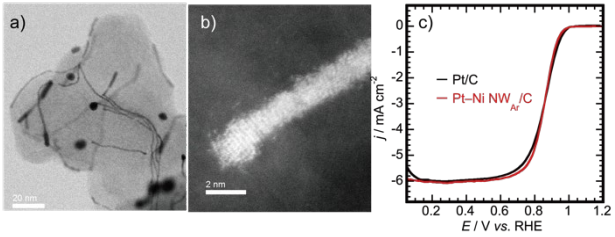

Figure 1. (a) STEM and (b) HAADF-STEM images of the as-prepared Pt–Ni NW_{Ar}/C and (c) LSVs of Pt–Ni NW_{Ar}/C (the trace in orange) and Pt/C (the trace in black) recorded at 1600 rpm at 10 mV s^{-1} in a positive-going sweep in a 0.1 M $HClO_4$ aqueous solution under oxygen. The LSVs were recorded after the electrochemical cleaning process.

Hydrodynamic voltammetry of NW_{Ar}/C after the electrochemical cleaning process was performed in a 0.1 M $HClO_4$ aqueous solution under oxygen to understand the ORR electrocatalytic activity. Linear sweep voltammograms (LSVs) of NW_{Ar}/C showed reduction currents under oxygen **(Figure 1c**) but not under Ar (**Figure S5**), indicating that the NWs show the electrocatalytic ORR activity. Electrochemically active surface areas of the NW_{Ar}/C based on the underpotential deposition of hydrogen ($ECSA_{updH}$) and the CO stripping voltammetry ($ECSA_{CO}$) were determined to be ca. 32 and 34 $m^2\ g_{Pt}^{-1}$, respectively. The initial mass activity (MA) and specific activity (SA) based on the $ECSA_{CO}$ for NW_{Ar}/C at 0.9 V vs. RHE were determined to be ca. 0.15 A $(mg_{Pt})^{-1}$ and 4.5 A m^{-2}, respectively, whereas the initial MA and SA of the Pt/C at 0.9 V vs. RHE were 0.11 A $(mg_{Pt})^{-1}$ and 1.4 A m^{-2}, respectively. Thus, the initial MA of NW_{Ar}/C was comparable or slightly higher than that of Pt/C.

To understand the durability of NW_{Ar}/C, LSVs of NW_{Ar}/C were recorded before (NW_{Ar}/C_0k) and after 25000 potential cycles (NW_{Ar}/C_25k) in the potential range between +0.6 and +1.0 V vs. RHE at 0.1 V s^{-1} in a 0.1 M $HClO_4$ aqueous solution under Ar (**Figure 2a**). In typical Pt-based ORR electrocatalysts including Pt/C, half-wave potentials ($E_{1/2}$) after the potential cycles were shifted to more negative potentials than that of the initial LSV because of the activity loss (**Figure S6**). Surprisingly, the $E_{1/2}$ of NW_{Ar}/C_25k was shifted to more positive potentials than that of NW_{Ar}/C_0 (**Figure 2a**). The MA, SA, and $ECSA_{CO}$ of NW_{Ar}/C_25k were determined to be 0.22 A $(mg_{Pt})^{-1}$ and 6.4 A m^{-2}, 35 $m^2\ g^{-1}$, respectively, indicating that the ORR activity tends to increase after 25k potential cycles. The MA and SA decreased after 50k potential cycles to 0.19 A $(mg_{Pt})^{-1}$ and 4.7 A m^{-2}, respectively. Note that a Pt:Ni atomic ratio was 95:5 and only 6.9% Pt was dissolved from NW_{Ar}/C even after 50k potential cycles while ca. 6.7% Pt was dissolved from Pt/C after 25k potential cycles. These results indicate that NW_{Ar}/C has a greater advantage to suppress the activity loss and dissolution of Pt than Pt/C.

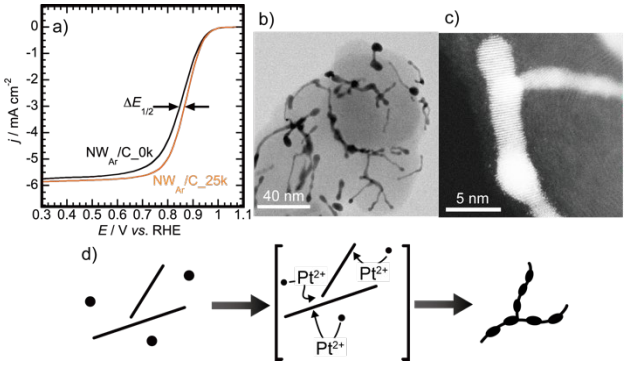

Figure 2. (a) LSVs of NW_{Ar}/C before (NW_{Ar}/C_0k in black) and after 25k potential cycles (NW_{Ar}/C_25k in orange). LSVs were

recorded at 1600 rpm and 10 mV s^{-1} in a 0.1 M $HClO_4$ aqueous solution under oxygen. The arrows indicate the $E_{1/2}$ difference ($\Delta E_{1/2}$). (b) STEM and (c) HAADF-STEM images of NW_{Ar}/C_25k. (d) Schematic representation of the structural transformation of NWs into a branched nanostructure assisted by Ostwald ripening of NPs.

To understand the origin of activity improvement and Pt dissolution suppression, STEM and HAADF-STEM images of NW_{Ar}/C after 25k potential cycles were taken. These images clearly indicate morphological transformation occurred from NWs to branched network structures (**Figures 2b** and **2c**). NWs were waved and connected to form branched nanostructures. Waved structures were more pronounced after 50k potential cycles (**Figure S7**), in comparison with NW_{Ar}/C_25k, and could be associated with the decrease of MA and SA after 50k potential cycles, as mentioned above. Our NW_{Ar}/C catalyst contains not only NWs but also NPs whereas previously reported NWs contain almost no NPs. Although durability tests of the NWs that contain almost no NPs were already performed,[9-10] such structural transformation has not been demonstrated even after ≥25k potential cycles. The morphological change could be mediated by dissolution/re-deposition of Pt from the co-present NPs rather than the agglomeration of NWs and NPs *via* the migration of NPs on the carbon support (**Figure 2d**) because of the coalescence in diameter[22-23] (**Figures 1b** and **2c**) and almost no NPs observed. This structural transformation highly likely induced the catalytic activity enhancement. Because it was previously reported that Pt NPs having large particle sizes are energetically stable and therefore durable against Pt dissolution,[23-24] the formation of the energetically stable branched nanostructure can contribute to the suppression of the Pt dissolution.

To understand the origin of the ORR activity enhancement, potential-dependent Pt L_3-edge X-ray absorption spectroscopy (XAS) of NW_{Ar}/C was performed before and after the 25k potential cycles in a fluorescent mode (**Figures 3a** and **3b**). In the X-ray absorption near edge structure (XANES) region, a white line peak was observed at ca. 11567 eV. This peak is associated with the 2p → 5d transition and white line intensities are known to be sensitive to changes in the oxidation state of Pt: higher white line intensities indicates higher oxidation states of Pt.[2,25-26] White line peak intensities of NW_{Ar}/C_0k (**Figures 3a** and **S8a**) and NW_{Ar}/C_25k (**Figure 3b** and **S8b**) were plotted against the potential (**Figure 3c**). Although a hysteresis is found for both plots, changes in intensities of NW_{Ar}/C_25k were smaller than those of NW_{Ar}/C_0k. This difference indicates that the formation of oxygenated Pt species such as $Pt(OH)_{ad}$ was suppressed after the potential cycles.[2,25,27-29] This suppression could be related to electronic structural changes of the surface Pt: for example, the downshift of the d-band center of the surface Pt[2-3] might be caused by a strain effect[30-31] and/or the formation of grain boundaries.[32-33] As a consequence, the ORR activity of NW_{Ar}/C_25k could be enhanced, compared with that of NW_{Ar}/C_0k. We also analyzed Fourier transforms (FT) of extended X-ray absorption fine structure (EXAFS) oscillations of the as-prepared NW_{Ar}/C recorded in a transmission mode and NW_{Ar}/C_25k in the fluorescent mode in the Pt L_3-edge region. The curve-fitting analysis of FT-EXAFS oscillations allowed us to determine Pt–Pt distances to be 2.74 ± 0.01 Å for the as-prepared NW_{Ar}/C and 2.73 ± 0.01 Å for NW_{Ar}/C_25k (**Table S1**). Furthermore, the periods of the oscillations of these samples are the same (**Figure S9**). Thus, 25k potential cycles gave significant differences in the surface susceptibility to $Pt(OH)_{ad}$ species but not in Pt–Pt distance of Pt–Ni NWs.

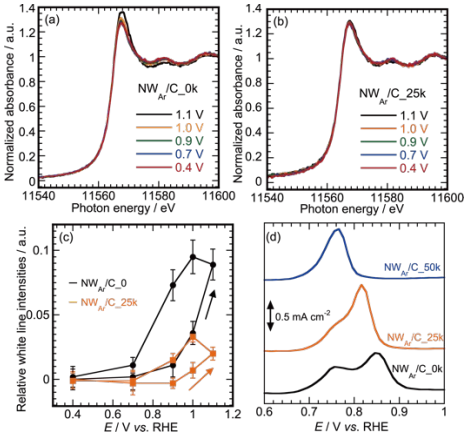

Figure 3. Potential dependent XANES spectra of (a) NW_{Ar}/C_0k and (b) NW_{Ar}/C_25k in the Pt L_3-edge region. (c) Relative white line peak intensities of NW_{Ar}/C_0k (in black) and NW_{Ar}/C_25k (in orange) against potential. Potentials were applied stepwise from +0.4 to +1.1 V and then +0.4 V vs. RHE. The spectra were collected in a 0.1 M $HClO_4$ aqueous solution under nitrogen in a fluorescent mode at the BL36XU station in SPring-8. (d) CO stripping voltammograms of NW_{Ar}/C_0k (the trace in black), NW_{Ar}/C_25k (the trace in orange) and NW_{Ar}/C_50k (the trace in blue) recorded at 50 mV s^{-1} in a 0.1 M $HClO_4$ aqueous solution under Ar. The voltammograms shown are the difference between the first and second cycles.

Electrochemical CO stripping voltammograms of NW_{Ar}/C before and after potential cycles also support surface structural changes induced by potential cycles. The CO oxidation was shifted to negative potentials after potential cycles: two peaks were observed at ca. 0.85 and 0.75 V vs. RHE for NW_{Ar}/C_0k, one peak at ca. 0.81 V and one shoulder peak at ca. 0.76 V for NW_{Ar}/C_25k, and one peak at ca. 0.76 V for NW_{Ar}/C_50k (**Figures 3d**). The peaks at ca. 0.85 V for NW_{Ar}/C_0k and at ca. 0.76 V for NW_{Ar}/C_50k could originate from NPs and the branched nanostructure, respectively. Because CO stripping peak positions are sensitive to surface structures and also known to be directly correlated with the position of the d-band center of the surface Pt,[2,10,34-36] the structural transformation to the branched nanostructure coupled with the formation of grain boundaries,[32-33] could lead to the activity enhancement.

Finally, to clarify the effect of the co-presence of NPs with NWs on the structural changes and activity, NP-free Pt–Ni NWs were prepared, and then their durability tests were performed (**Figure S10**). NP-free NWs were prepared in the air (NW_{air}) and then loaded on the carbon black of Vulcan XC-72 (NW_{air}/C, See the SI). STEM images of the as-prepared NW_{air}/C confirmed the formation of NWs with 1.65±0.02 nm in diameter and 23±1 nm in length without almost no NPs (**Figure 4a**). The use of the air containing oxygen as the

synthetic atmosphere enables us to obtain NWs exclusively. The Pt:Ni atomic ratio for the as-prepared NW_{air} was determined to be 95:5, which was almost the same as that of NW_{Ar} with NPs after the electrochemical cleaning (NW_{Ar}_0k). Thus, not only the exclusive NW formation but also the Ni content were sensitive to the synthetic atmosphere. MAs and SAs based on $ECSA_{CO}$ for NW_{air}/C at 0.9 V vs. RHE were determined to be 0.23 A $(mg_{Pt})^{-1}$ and 4.7 A m^{-2} before potential cycles (NW_{air}/C_0k), 0.24 A $(mg_{Pt})^{-1}$ and 4.3 A m^{-2} after 25 k potential cycles (NW_{air}/C_25k), and 0.21 A $(mg_{Pt})^{-1}$ and 4.4 A m^{-2} for NW_{air}/C after at 50k potential cycles (NW_{air}/C_50k). The Pt:Ni atomic ratio of 95:5 remained for NW_{air}/C_50k, confirmed by ICP-MS. Over the potential cycles of NP-free NW_{air}/C, the structural transformation to the branched nanostructure was also observed (**Figure 4b**).

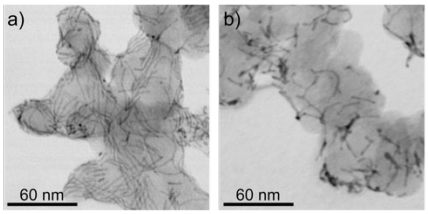

Figure 4. STEM images of (a) the as-prepared NP-free NW/C (NW_{air}/C) and (b) NP-free NW_{air}/C_50k.

The CO stripping voltammogram of NW_{air}/C_50k showed a peak at ca. 0.75 V vs. RHE (**Figure S11**), which is the same as that for NW_{Ar}/C_50k (**Figures 3d**), indicating that the potential cycles of NW_{air}/C and NW_{Ar}/C gave the branched nanostructure with the similar surface state. Interestingly, CO stripping voltammograms of NW_{Ar}/C_0k and NW_{air}_0k are different, which indicates that the surface Pt of NW_{Ar}/C_0k produced by the electrochemical cleaning (dealloying) process can be different from the surface Pt of NW_{air}_0k produced in the presence of oxygen during the synthesis. Furthermore, 50k potential cycles caused ca. 15% Pt dissolution for NW_{air}/C, which is much larger than that of NW_{Ar}/C (6.9% as mentioned above). These results indicate that the co-presence of NPs with NWs has an important role in the suppression of Pt dissolution but not the structural transformation of NWs to the branched nanostructure.

In conclusion, we prepared the Pt–Ni NWs with and without NPs as ORR electrocatalysts and investigated their structural and electronic changes after potential cycles. The NWs were transformed into branched nanostructures during potential cycles. *In situ* XAS and electrochemical CO stripping measurements revealed that the electronic structure of the surface Pt was changed by the structural transformation and then the metal oxide formation at the NW surface seems to be suppressed, resulting in the high durability. Although the structural transformation can be observed both in the presence and absence of NPs, the Ostwald ripening of NPs assisted the structural transformation of NWs to the branched nanostructure, which is energetically stable and therefore durable against Pt dissolution. This work demonstrated that such Ostwald-ripening-assisted structural transformations can, in principle, be utilized for not only NWs but also other nanostructured catalysts, allowing us to design and develop highly active and durable Pt-based electrocatalysts for many electrocatalytic reactions including the ORR and phase-engineered nanomaterials.[32-33]

ASSOCIATED CONTENT

AUTHOR INFORMATION

Corresponding Author

*masaru.kato@ees.hokudai.ac.jp (MK); iyagi@ees.hokudai.ac.jp (IY)

Supporting Information

The Supporting Information is available free of charge on the ACS Publications website.
Experimental section, size distribution of NWs and NPs, HAADF-STEM images, EDS mapping, XRD patterns, CVs under Ar, LSVs of Pt/C, XANES spectra, EXAFS oscillations, CO stripping voltammograms, and parameters used for EXAFS curve-fitting analysis (PDF)

ACKNOWLEDGMENTS

The authors thank Shingo Mukai, Yusuke Kawamura (Technical Division, Institute for Catalysis, Hokkaido University) and Takao Ohta (Graduate School of Engineering, Hokkaido University) for their technical support on electrochemical setups; Naomi Hirai (Research Institute for Electronic Science, Hokkaido University) for taking the HAADF–STEM and EDS mapping images; Dr. Kiyonori Takahashi and Prof. Takayoshi Nakamura for taking XRD patterns; and Dr. Yohei Uemura (Paul Scherrer Institut) and Prof. Yasuhiro Iwasawa (The University of Electro-Communications) for fruitful discussion on XAS measurements and data analysis.

This work was supported by the project "Development of Advanced PEFC Utilization Technologies/Development of Fundamental Technologies for PEFC Promotion/Highly-Coupled Analysis of Phenomena in MEA and its Constituents and Evaluation of Cell Performance" of NEDO, Japan and "Nanotechnology Platform" Program of the Ministry of Education, Culture, Sports, Science and Technology (MEXT) for Hokkaido University (Grant numbers: JPMXP09A17HK0073, 18HK0063, 19HK0030 and 21HK0062). XAS experiments were performed at the beamline BL36XU, SPring-8, Japan (Proposal Nos. 2018A7903, 2019A7903, and 2019B7903) and the beamlines BL5S1 and BL11S2, AichiSR (Proposal Nos. 202004012 and 202004064), japan.

ABBREVIATIONS

NW_{Ar}, nanowire prepared under Ar; NP, nanoparticle; NW_{Ar}/C, the as-prepared NW_{Ar} supported on Vulcan XC-72; NW_{Ar}/C_0k, NW_{Ar}/C just after the electrochemical cleaning process; NW_{Ar}/C_25k, NW_{Ar}/C after 25000 potential cycles; NW_{Ar}/C_50k, NW_{Ar}/C after 50000 potential cycles; NW_{air}, nanowire prepared under the air; XAS, X-ray absorption spectroscopy; XANES, X-ray absorption near-edge structure; EXAFS, extended X-ray absorption fine structure.

REFERENCES

1. Wang, X.; Vara, M.; Luo, M.; Huang, H.; Ruditskiy, A.; Park, J.; Bao, S.; Liu, J.; Howe, J.; Chi, M.; Xie, Z.; Xia, Y. Pd@Pt Core–Shell Concave Decahedra: A Class of Catalysts for the Oxygen Reduction Reaction with Enhanced Activity and Durability. *J. Am. Chem. Soc.* **2015**, *137*, 15036-15042. DOI: 10.1021/jacs.5b10059.

2. Kato, M.; Nakahoshiba, R.; Ogura, K.; Tokuda, S.; Yasuda, S.; Higashi, K.; Uruga, T.; Uemura, Y.; Yagi, I. Electronic Effects of Nitrogen Atoms of Supports on Pt–Ni Rhombic Dodecahedral Nanoframes for Oxygen Reduction. *ACS Appl. Energy Mater.* **2020**, *3*, 6768-6774. DOI: 10.1021/acsaem.0c00903.

3. Kato, M.; Ogura, K.; Nakagawa, S.; Tokuda, S.; Takahashi, K.; Nakamura, T.; Yagi, I. Enhancement of Electrocatalytic Oxygen Reduction Activity and Durability of Pt–Ni Rhombic Dodecahedral Nanoframes by Anchoring to Nitrogen-Doped Carbon Support. *ACS Omega* **2018**, *3*, 9052-9059. DOI: 10.1021/acsomega.8b01373.

4. Chen, C.; Kang, Y. J.; Huo, Z. Y.; Zhu, Z. W.; Huang, W. Y.; Xin, H. L. L.; Snyder, J. D.; Li, D. G.; Herron, J. A.; Mavrikakis, M.; Chi, M. F.; More, K. L.; Li, Y. D.; Markovic, N. M.; Somorjai, G. A.; Yang, P. D.; Stamenkovic, V. R. Highly Crystalline Multimetallic Nanoframes with Three-Dimensional Electrocatalytic Surfaces. *Science* **2014**, *343*, 1339-1343. DOI: 10.1126/science.1249061.

5. Kwon, T.; Jun, M.; Lee, K. Catalytic Nanoframes and Beyond. *Adv. Mater.* **2020**, *32*, 2001345. DOI: https://doi.org/10.1002/adma.202001345.

6. Yang, T.-H.; Ahn, J.; Shi, S.; Wang, P.; Gao, R.; Qin, D. Noble-Metal Nanoframes and Their Catalytic Applications. *Chem. Rev.* **2021**, *121*, 796-833. DOI: 10.1021/acs.chemrev.0c00940.

7. Li, M.; Zhao, Z.; Cheng, T.; Fortunelli, A.; Chen, C.-Y.; Yu, R.; Zhang, Q.; Gu, L.; Merinov, B. V.; Lin, Z.; Zhu, E.; Yu, T.; Jia, Q.; Guo, J.; Zhang, L.; Goddard, W. A.; Huang, Y.; Duan, X. Ultrafine jagged platinum nanowires enable ultrahigh mass activity for the oxygen reduction reaction. *Science* **2016**, *354*, 1414-1419. DOI: 10.1126/science.aaf9050.

8. Sun, Y.; Luo, M.; Qin, Y.; Zhu, S.; Li, Y.; Xu, N.; Meng, X.; Ren, Q.; Wang, L.; Guo, S. Atomic-Thick PtNi Nanowires Assembled on Graphene for High-Sensitivity Extracellular Hydrogen Peroxide Sensors. *ACS Appl. Mater. Interf.* **2017**, *9*, 34715-34721. DOI: 10.1021/acsami.7b11758.

9. Jiang, K.; Zhao, D.; Guo, S.; Zhang, X.; Zhu, X.; Guo, J.; Lu, G.; Huang, X. Efficient oxygen reduction catalysis by subnanometer Pt alloy nanowires. *Sci. Adv.* **2017**, *3*, e1601705. DOI: 10.1126/sciadv.1601705.

10. Kong, F.; Norouzi Banis, M.; Du, L.; Zhang, L.; Zhang, L.; Li, J.; Doyle-Davis, K.; Liang, J.; Liu, Q.; Yang, X.; Li, R.; Du, C.; Yin, G.; Sun, X. Highly stable one-dimensional Pt nanowires with modulated structural disorder towards the oxygen reduction reaction. *J. Mater. Chem. A* **2019**, *7*, 24830-24836. DOI: 10.1039/C9TA08120H.

11. Bu, L.; Guo, S.; Zhang, X.; Shen, X.; Su, D.; Lu, G.; Zhu, X.; Yao, J.; Guo, J.; Huang, X. Surface engineering of hierarchical platinum-cobalt nanowires for efficient electrocatalysis. *Nat. Commun.* **2016**, *7*, 11850. DOI: 10.1038/ncomms11850.

12. Gong, M.; Deng, Z.; Xiao, D.; Han, L.; Zhao, T.; Lu, Y.; Shen, T.; Liu, X.; Lin, R.; Huang, T.; Zhou, G.; Xin, H.; Wang, D. One-Nanometer-Thick Pt3Ni Bimetallic Alloy Nanowires Advanced Oxygen Reduction Reaction: Integrating Multiple Advantages into One Catalyst. *ACS Catal.* **2019**, *9*, 4488-4494. DOI: 10.1021/acscatal.9b00603.

13. Yoon, J.; Park, J.; Sa, Y. J.; Yang, Y.; Baik, H.; Joo, S. H.; Lee, K. Synthesis of bare Pt3Ni nanorods from PtNi@Ni core–shell nanorods by acid etching: one-step surfactant removal and phase conversion for optimal electrochemical performance toward oxygen reduction reaction. *CrystEngComm* **2016**, *18*, 6002-6007. DOI: 10.1039/C6CE00830E.

14. Li, F.; Medvedeva, X. V.; Medvedev, J. J.; Khairullina, E.; Engelhardt, H.; Chandrasekar, S.; Guo, Y.; Jin, J.; Lee, A.; Thérien-Aubin, H.; Ahmed, A.; Pang, Y.; Klinkova, A. Interplay of electrochemical and electrical effects induces structural transformations in electrocatalysts. *Nat. Catal.* **2021**, *4*, 479-487. DOI: 10.1038/s41929-021-00624-y.

15. Hodnik, N.; Dehm, G.; Mayrhofer, K. J. J. Importance and Challenges of Electrochemical in Situ Liquid Cell Electron Microscopy for Energy Conversion Research. *Acc. Chem. Res.* **2016**, *49*, 2015-2022. DOI: 10.1021/acs.accounts.6b00330.

16. Chen, K.-C.; Wu, W.-W.; Liao, C.-N.; Chen, L.-J.; Tu, K. N. Observation of Atomic Diffusion at Twin-Modified Grain Boundaries in Copper. *Science* **2008**, *321*, 1066-1069. DOI: 10.1126/science.1160777.

17. Zhao, Z.; Chen, C.; Liu, Z.; Huang, J.; Wu, M.; Liu, H.; Li, Y.; Huang, Y. Pt-Based Nanocrystal for Electrocatalytic Oxygen Reduction. *Adv. Mater.* **2019**, *31*, 1808115. DOI: https://doi.org/10.1002/adma.201808115.

18. Wang, C.; Hou, Y.; Kim, J.; Sun, S. A General Strategy for Synthesizing FePt Nanowires and Nanorods. *Angew. Chem. Int. Ed.* **2007**, *46*, 6333-6335. DOI: https://doi.org/10.1002/anie.200702001.

19. Xu, H.; Wei, J.; Zhang, M.; Wang, C.; Shiraishi, Y.; Guo, J.; Du, Y. Solvent-mediated length tuning of ultrathin platinum–cobalt nanowires for efficient electrocatalysis. *J. Mater. Chem. A* **2018**, *6*, 24418-24424. DOI: 10.1039/C8TA08251K.

20. Bu, L.; Ding, J.; Guo, S.; Zhang, X.; Su, D.; Zhu, X.; Yao, J.; Guo, J.; Lu, G.; Huang, X. A General Method for Multimetallic Platinum Alloy Nanowires as Highly Active and Stable Oxygen Reduction Catalysts. *Adv. Mater.* **2015**, *27*, 7204-7212. DOI: https://doi.org/10.1002/adma.201502725.

21. Petkov, V.; Maswadeh, Y.; Vargas, J. A.; Shan, S.; Kareem, H.; Wu, Z.-P.; Luo, J.; Zhong, C.-J.; Shastri, S.; Kenesei, P. Deviations from Vegard's law and evolution of the electrocatalytic activity and stability of Pt-based nanoalloys inside fuel cells by in operando X-ray spectroscopy and total scattering. *Nanoscale* **2019**, *11*, 5512-5525. DOI: 10.1039/C9NR01069F.

22. Padgett, E.; Yarlagadda, V.; Holtz, M. E.; Ko, M.; Levin, B. D. A.; Kukreja, R. S.; Ziegelbauer, J. M.; Andrews, R. N.; Ilavsky, J.; Kongkanand, A.; Muller, D. A. Mitigation of PEM Fuel Cell Catalyst Degradation with Porous Carbon Supports. *J. Electrochem. Soc.* **2019**, *166*, F198-F207. DOI: 10.1149/2.0371904jes.

23. Kobayashi, A.; Fujii, T.; Harada, C.; Yasumoto, E.; Takeda, K.; Kakinuma, K.; Uchida, M. Effect of Pt and Ionomer Distribution on Polymer Electrolyte Fuel Cell Performance and Durability. *ACS Appl. Energy Mater.* **2021**, *4*, 2307-2317. DOI: 10.1021/acsaem.0c02841.

24. Uchida, M.; Park, Y.-C.; Kakinuma, K.; Yano, H.; Tryk, D. A.; Kamino, T.; Uchida, H.; Watanabe, M. Effect of the state of distribution of supported Pt nanoparticles on effective Pt utilization in polymer electrolyte fuel cells. *Phys. Chem. Chem. Phys.* **2013**, *15*, 11236-11247. DOI: 10.1039/C3CP51801A.

25. Nagasawa, K.; Takao, S.; Nagamatsu, S.-i.; Samjeské, G.; Sekizawa, O.; Kaneko, T.; Higashi, K.; Yamamoto, T.; Uruga, T.; Iwasawa, Y. Surface-Regulated Nano-SnO2/Pt3Co/C Cathode Catalysts for Polymer Electrolyte Fuel Cells Fabricated by a Selective Electrochemical Sn Deposition Method. *J. Am. Chem. Soc.* **2015**, *137*, 12856-12864. DOI: 10.1021/jacs.5b04256.

26. Sinfelt, J. H.; Meitzner, G. D. X-ray absorption edge studies of the electronic structure of metal catalysts. *Acc. Chem. Res.* **1993**, *26*, 1-6. DOI: 10.1021/ar00025a001.

27. Lee, S. W.; Chen, S.; Suntivich, J.; Sasaki, K.; Adzic, R. R.; Shao-Horn, Y. Role of Surface Steps of Pt Nanoparticles on the Electrochemical Activity for Oxygen Reduction. *J. Phys. Chem. Lett.* **2010**, *1*, 1316-1320. DOI: 10.1021/jz100241j.

28. Zhao, X.; Takao, S.; Higashi, K.; Kaneko, T.; Samjeske, G.; Sekizawa, O.; Sakata, T.; Yoshida, Y.; Uruga, T.; Iwasawa, Y. Simultaneous Improvements in Performance and Durability of an Octahedral PtNix/C Electrocatalyst for Next-Generation Fuel Cells by Continuous, Compressive, and Concave Pt Skin Layers. *ACS Catal.* **2017**, *7*, 4642-4654. DOI: 10.1021/acscatal.7b00964.

29. Tian, X.; Zhao, X.; Su, Y.-Q.; Wang, L.; Wang, H.; Dang, D.; Chi, B.; Liu, H.; Hensen, E. J. M.; Lou, X. W.; Xia, B. Y. Engineering bunched Pt-Ni alloy nanocages for efficient oxygen reduction in practical fuel cells. *Science* **2019**, *366*, 850-856. DOI: 10.1126/science.aaw7493.

30. Hernandez-Fernandez, P.; Masini, F.; McCarthy, D. N.; Strebel, C. E.; Friebel, D.; Deiana, D.; Malacrida, P.; Nierhoff, A.; Bodin, A.; Wise, A. M.; Nielsen, J. H.; Hansen, T. W.; Nilsson, A.; Stephens, I. E.

L.; Chorkendorff, I. Mass-selected nanoparticles of PtxY as model catalysts for oxygen electroreduction. *Nat. Chem.* **2014**, *6*, 732-738. DOI: 10.1038/nchem.2001.

31. Brandiele, R.; Guadagnini, A.; Girardi, L.; Dražić, G.; Dalconi, M. C.; Rizzi, G. A.; Amendola, V.; Durante, C. Climbing the oxygen reduction reaction volcano plot with laser ablation synthesis of PtxY nanoalloys. *Catal. Sci. Technol.* **2020**, *10*, 4503-4508. DOI: 10.1039/D0CY00983K.

32. Li, H.; Zhou, X.; Zhai, W.; Lu, S.; Liang, J.; He, Z.; Long, H.; Xiong, T.; Sun, H.; He, Q.; Fan, Z.; Zhang, H. Phase Engineering of Nanomaterials for Clean Energy and Catalytic Applications. *Adv. Energy Mater.* **2020**, *10*, 2002019. DOI: https://doi.org/10.1002/aenm.202002019.

33. Lu, S.; Liang, J.; Long, H.; Li, H.; Zhou, X.; He, Z.; Chen, Y.; Sun, H.; Fan, Z.; Zhang, H. Crystal Phase Control of Gold Nanomaterials by Wet-Chemical Synthesis. *Acc. Chem. Res.* **2020**, *53*, 2106-2118. DOI: 10.1021/acs.accounts.0c00487.

34. Jiang, T.; Mowbray, D. J.; Dobrin, S.; Falsig, H.; Hvolbæk, B.; Bligaard, T.; Nørskov, J. K. Trends in CO Oxidation Rates for Metal Nanoparticles and Close-Packed, Stepped, and Kinked Surfaces. *J. Phys. Chem. C* **2009**, *113*, 10548-10553. DOI: 10.1021/jp811185g.

35. Hammer, B.; Nielsen, O. H.; Nrskov, J. K. Structure sensitivity in adsorption: CO interaction with stepped and reconstructed Pt surfaces. *Catal. Lett.* **1997**, *46*, 31-35. DOI: 10.1023/A:1019073208575.

36. Chattot, R.; Martens, I.; Scohy, M.; Herranz, J.; Drnec, J.; Maillard, F.; Dubau, L. Disclosing Pt-Bimetallic Alloy Nanoparticle Surface Lattice Distortion with Electrochemical Probes. *ACS Energy Lett.* **2020**, *5*, 162-169. DOI: 10.1021/acsenergylett.9b02287.

SYNOPSIS TOC